Journal of Materials Chemistry A

PAPER

View Article Online
View Journal | View Issue

Cite this: J. Mater. Chem. A, 2019, 7, 1638

Facile synthesis and characterization of $Bi_{13}S_{18}I_2$ films as a stable supercapacitor electrode material†

Keir Adams,‡[a] Alba Franco González,‡[a] John Mallows,[a] Tianyue Li, *[a] Job H. J. Thijssen [b] and Neil Robertson *[a]

Received 16th November 2018
Accepted 20th December 2018

DOI: 10.1039/c8ta11029h

rsc.li/materials-a

Electrical double layer capacitors (EDLCs) featuring low-cost and solution-processable electrode materials have attracted significant research interest for their green and economical applications in energy harvesting and storage devices. Here, we demonstrate a novel synthetic route for films of an underexplored 3-D hexagonal bismuth chalcohalide, $Bi_{13}S_{18}I_2$, and investigate its potential as the active electrode material in EDLC-type supercapacitors. The synthetic procedure has been optimised and comprises the lowest annealing temperature (150 °C) and the shortest processing time (1 h) currently reported. When integrated in a symmetrical EDLC with an aqueous $NaClO_4$ electrolyte, the $Bi_{13}S_{18}I_2$-based device achieves a remarkable areal capacitance of 210.68 mF cm^{-2} with 99.7% capacitance retention after 5000 cycles. Both the $Bi_{13}S_{18}I_2$ powder and thin-film electrodes have been characterized through XRD, XPS, Raman spectroscopy, and SEM. The superior stability, low-cost, and facile synthesis of $Bi_{13}S_{18}I_2$ proves its promising potential for supercapacitor applications.

Introduction

Demand for efficient, economic, and eco-friendly energy storage systems has grown dramatically in recent years for applications in electronic appliances, electric vehicles, and a smart and sustainable energy grid.[1–3] Given the high production costs and environmental hazards of conventional energy storage technologies, researchers have focused on developing novel energy materials and optimising their performance in electronic devices.[4–8] In particular, interest has grown in high-Z ns^2 cations with an electronic configuration of $[Xe]6S^2 5p^0$.[9,10] Among these main group cations, bismuth has attracted considerable attention because of its low-toxicity and structural-diversity.[11,12] For example, bismuth-based perovskite-like materials have been well-studied in applications such as lead-free photovoltaic devices, radiation detectors, and supercapacitor electrodes.[13–20] Among the inorganic bismuth-based materials, bismuth chalcogenides and chalcohalides have captured research interests for their manifold functionalities in photocatalysis,[21–23] photovoltaics,[24] and radiation detection.[25,26] Bi_2O_3 and Bi_2S_3 have already proven their promising potential in photocatalytic water purification, thermoelectric systems, supercapacitors, and electrochemical sensors.[21,27–29] Bi_2S_3 has also displayed remarkably varied crystal morphologies, including nanorods, nanobelts, and microflowers, which can be tuned for enhanced performance as the active electrode material in supercapacitors.[30,31] Among the common Bi-based chalcohalides, BiSI and BiSeI have been studied as potential photovoltaic materials due to their n-type semiconducting properties and high absorption coefficients,[32,33] while both theoretical and experimental studies have evaluated their promise in radiation detection. Still, despite BiSI's exhibition of strong photocurrent,[34] such Bi-chalcohalides have yet to yield satisfactory photovoltaic performance in solar cells.[32] Moreover, the fabrication of bismuth chalcohalides typically requires high annealing temperatures and laborious, multistep procedures, complicating research efforts and economic viability. To the best of our knowledge, no simple, one-step, solution-processing synthetic route has been reported.

Electrical double-layer capacitors (EDLCs) are best known for their fast charge–discharge cycles, high power densities, long life cycles, and greater energy densities compared to conventional capacitors. However, EDLCs typically suffer from poorer energy densities compared to so-called pseudo-capacitors or conventional batteries that employ strong faradaic reactions to chemically store charge.[35] Consequently, there has been a recent wave of research efforts directed toward advancing the energy densities of environmentally-benign, economical, and durable electrode materials for EDLC applications in order to enhance their commercial viability without sacrificing long-life

[a]School of Chemistry, EaStCHEM, University of Edinburgh, King's Buildings, David Brewster Road, Edinburgh, Scotland EH9 3FJ, UK. E-mail: Neil.Robertson@ed.ac.uk; Tianyue.Li@ed.ac.uk

[b]SUPA School of Physics & Astronomy, University of Edinburgh, Edinburgh, EH9 3FD, UK

† Electronic supplementary information (ESI) available: XRD spectra of different layers, SEM images, Raman, and IR spectra of electrode after cycles; Bode plot, frequency *vs.* Z″ and Nyquist plot before and after 5000 cycles. See DOI: 10.1039/c8ta11029h

‡ These authors contributed equally to this work.

cycle stability. In this respect, bismuth chalcogenides including Bi_2S_3 and Bi_2O_3 have been widely studied and applied as high-performing active electrode materials intended as supercapacitors, albeit typically with substantial faradaic mechanism.[36] On the other hand, bismuth chalcohalides have often been overlooked as potential energy storage materials. In this study, a relatively unexplored bismuth chalcohalide material, $Bi_{13}S_{18}I_2$, has been synthesised from solution in a single and facile step. Traditionally, such materials are fabricated under high pressure and high temperature conditions requiring long reaction times.[37–39] Using our easily synthesised $Bi_{13}S_{18}I_2$ as the active material in EDLC-type supercapacitors, we have achieved a device areal capacitance of 210.68 mF cm^{-2}, a specific capacitance of 6.58 F g^{-1}, and superior cycle stability with 99.7% capacitance retention even after 5000 cycles.

Results and discussion

Material characterization

Synthesis. $Bi_{13}S_{18}I_2$ was synthesised *via* thermal decomposition of a precursor solution containing bismuth xanthate ($Bi(xt)_3$), a sulfur-containing organobismuth material, and BiI_3. $Bi(xt)_3$ was synthesized from potassium xanthate and bismuth nitrate in a one-step reaction previously reported by Vigneshwaran and colleagues.[40] A wide range of $Bi(xt)_3$: BiI_3 ratios from 2 : 1 to 26 : 1 were tested and spin-coated on quartz glass, forming a thin film which was subsequently annealed at 150 °C on a hot plate. The annealing temperature for the thin films was set slightly higher than the decomposition temperature of xanthate to ensure reaction completion (Scheme 1).

Structural and electronic characterization. The diffraction patterns obtained for thin films with 2 : 1, 10 : 1, and 18 : 1 ratios of the $Bi(xt)_3$: BiI_3 precursor solution are recorded in Fig. 1. A crystallographic XRD pattern corresponding to $Bi_{13}S_{18}I_2$ was identified in each of the three spectra. The 2 : 1 ratio produces the pattern with the lowest peak intensity, attributed to the stoichiometric mismatch of the precursor solution. In contrast, using a 26 : 1 solution produced a thin film with XRD (Fig. S2†) displaying both $Bi_{13}S_{18}I_2$ and Bi_2S_3 crystal peaks, suggesting that the sulfur concentration of the precursor solution was too high. Under these considerations, a 18 : 1 $Bi(xt)_3$: BiI_3 ratio was ultimately selected for further syntheses and characterization of the thin films. We note that $Bi_{13}S_{18}I_2$ has been previously reported as $[Bi(Bi_2S_3)_9I_3]_{2/3}$ (ref. 38) and $Bi_{19}S_{27}I_3$,[39] prompting Groom and colleagues to reconsider the crystal structure and propose the formula $Bi_{13}S_{18}I_2$,[41] which we adopt in our study. $Bi_{13}S_{18}I_2$ contains $[Bi_2]^{4+}$ dimers, which justifies the close proximity of the bismuth cations positioned at the origin of the unit cell (Fig. 2).

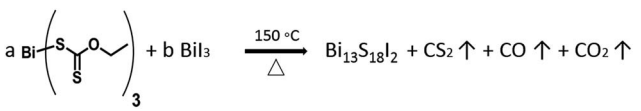

Scheme 1 Synthesis of $Bi_{13}S_{18}I_2$ from different ratios (a : b) of a $Bi(xt)_3$: BiI_3 precursor solution.

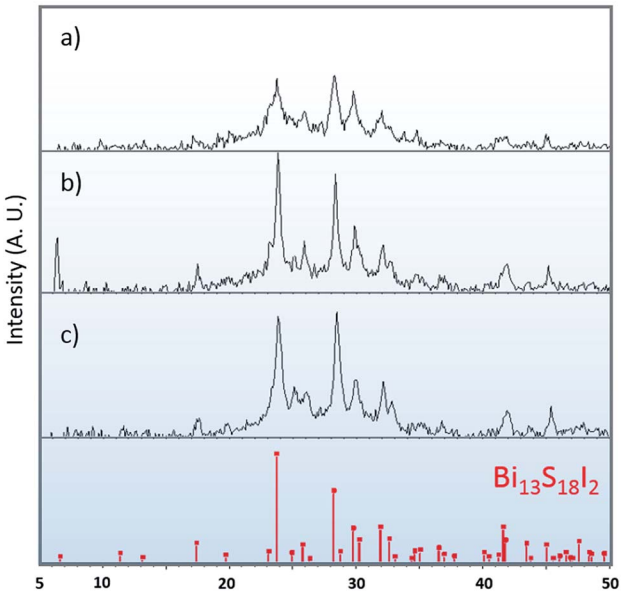

Fig. 1 XRD for thin films synthesized from precursor solutions with (a) 2 : 1, (b) 10 : 1, and (c) 18 : 1 $Bi(xt)_3$: BiI_3 ratios. The calculated XRD pattern of $Bi_{13}S_{18}I_2$.

We also evaluated the effect of film thickness on the crystallographic patterns. The XRD for thin films comprised of 1, 3, and 5 layers are displayed in Fig. S3† and the characteristic $Bi_{13}S_{18}I_2$ pattern is most clearly identified with the samples containing 3 and 5 layers. Fig. 3 displays the SEM images of the as-prepared $Bi_{13}S_{18}I_2$. As the number of layers increases, the nano-particle crystals grow longer tubule-like nano-rod structures approaching 250 nm in length. This suggests that increased surface area may be achieved by multiple-layer deposition of $Bi_{13}S_{18}I_2$ during the thin-film formation. We attempted to carry out BET isotherm determination of the surface area, however this is not possible on thin films of such small mass.

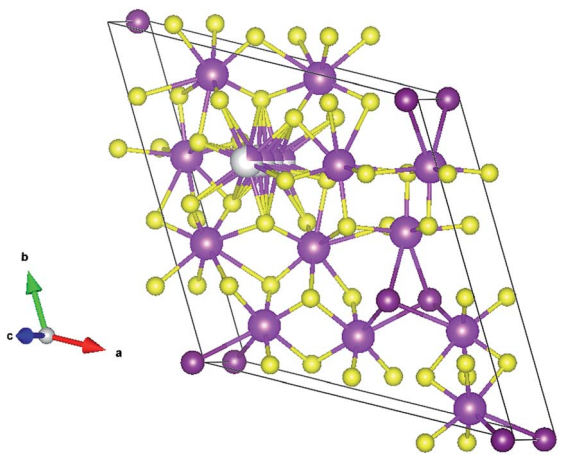

Fig. 2 Crystallographic packing diagram of $Bi_{13}S_{18}I_2$ unit cell, bismuth: magenta; iodine: purple; sulfur: yellow. The disordered bismuth is shown in grey/magenta with an occupancy factor of 0.25.

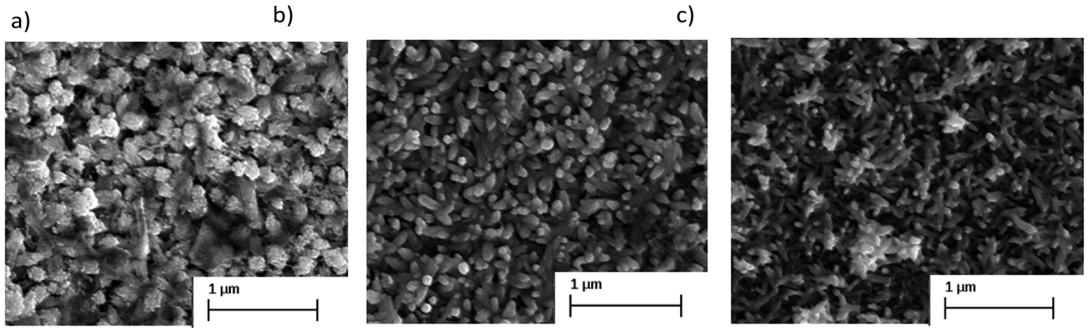

Fig. 3 SEM images for (a) one, (b) three, and (c) five layers of $Bi_{13}S_{18}I_2$ on conductive FTO glass substrate.

Fig. 4 depicts the X-ray photoelectron spectra (XPS) of an 18 : 1 thin film on FTO-coated glass with a mesoporous TiO_2 layer, and Table 1 tabulates the observed experimental atomic percentages of specific bismuth, iodine, and sulfur in the film. The values agree closely with the theoretical atomic composition of $Bi_{13}S_{18}I_2$. Diffuse reflectance measurements were also conducted to obtain the optical band gap of $Bi_{13}S_{18}I_2$ in its solid state. An indirect energy gap ($E_{g_{ind}}$) of 0.75 eV and a direct energy gap ($E_{g_{dir}}$) of 0.91 eV were estimated, which compare well with the literature values in Table S1.† Furthermore, we performed cyclic voltammetry (CV) measurements on a thin film sample spin-coated on FTO as the working electrode to evaluate the electrochemical behaviour of $Bi_{13}S_{18}I_2$. The cyclic voltammograms in Fig. S4† represent an average of 5 cycles at a sweep velocity of 0.1 V s^{-1}. The full CV scans indicate that $Bi_{13}S_{18}I_2$ undergoes irreversible redox processes, and the ionization potential (IP) can be estimated using the oxidation potential E^{ox} against the Ag/AgCl electrode (4.4 ± 0.1 eV below vacuum-level).[42] The electronic band gap of solid-state $Bi_{13}S_{18}I_2$ is estimated to be 0.99 V for the sample sweep at 0.1 V s^{-1}, calculated from the difference in E_{pa} and E_{pc} values and consistent with diffuse reflectance (Fig. 5).

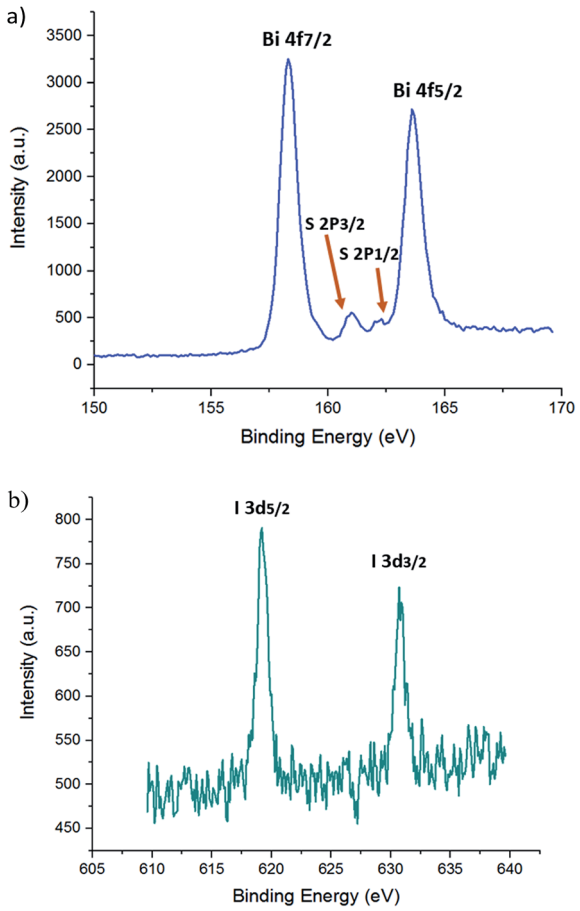

Fig. 4 High resolution X-ray photoelectron spectrum of Bi 4f, S 2p (a), I 5d (b) for a thin $Bi_{13}S_{18}I_2$ film. Specific peaks are labelled with their corresponding electronic orbitals.

Supercapacitor studies

Electrode preparation. The performance of $Bi_{13}S_{18}I_2$ as the active electrode material in an EDLC-type symmetric supercapacitor was evaluated using cyclic voltammetry (CV), galvanostatic charge–discharge, and electrochemical impedance spectroscopy (EIS). The $Bi_{13}S_{18}I_2$-based electrodes were fabricated with a facile, single-step, and solution-processable procedure. An 18 : 1 mixture of $Bi(xt)_3$ and BiI_3 was combined with activated charcoal and polytetrafluoroethylene (PTFE) powder and dispersed in DMF in sufficient relative amounts to form a 85 : 10 : 5 weight ratio of $Bi_{13}S_{18}I_2$: charcoal : PTFE upon subsequent thermal decomposition of the $Bi(xt)_3$. This heterogeneous solution was then drop-cast on 1 cm^2 sections of carbon cloth and heated at 150 °C to achieve a high mass loading of approximately 8–10 mg cm^{-2} on each electrode. Although the $Bi_{13}S_{18}I_2$ constitutes the primary active material for the supercapacitor electrodes, the activated charcoal and

Table 1 Atomic percentages of elements present in thin film shown by XPS compared with theoretical values in $Bi_{13}S_{18}I_2$

Element/orbital	At%	Total	At% in $Bi_{13}S_{18}I_2$
Bi/4d 3	18.16	38.52	39.39
Bi/4d 5	20.36		
I/3d 3	3.81	7.97	6.06
I/3d 5	4.16		
5/2s	53.42	53.42	54.55

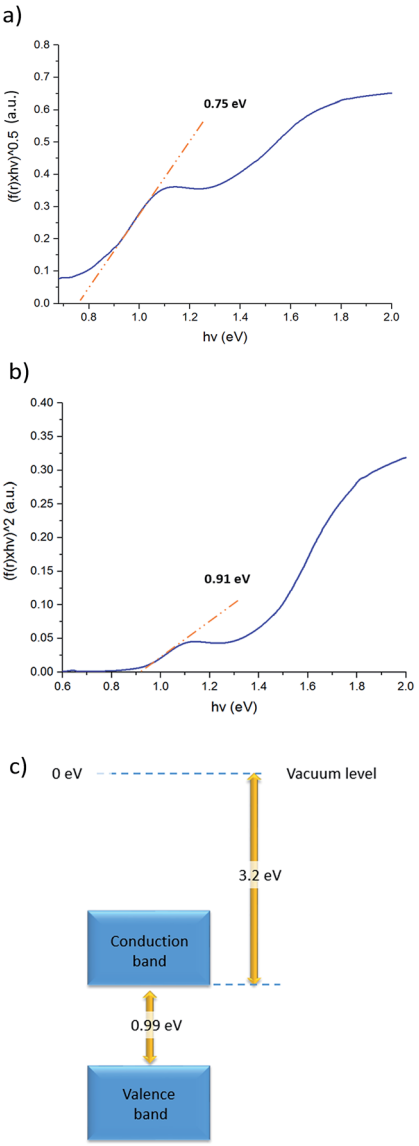

Fig. 5 Tauc plots for the estimation of direct (a) and indirect (b) band gaps of $Bi_{13}S_{18}I_2$. (c) Schematic diagram of the energy levels of $Bi_{13}S_{18}I_2$, estimated from electrochemistry measurements.

PTFE are added for enhanced electrical conductivity and mechanical stability respectively of the overall layer. The powder XRD pattern of as-prepared $Bi_{13}S_{18}I_2$ electrode is shown in Fig. 6, and the crystallite size of $Bi_{13}S_{18}I_2$ is calculated to be around 5 nm according to the Scherrer equation. The SEM images of the as-prepared electrodes show good coverage of the underlying carbon cloth with the activated $Bi_{13}S_{18}I_2$ material, with rod-shaped $Bi_{13}S_{18}I_2$ layering on top of the carbon cloth as well as binding directly to the carbon fibres (Fig. 7b). A thin (25 μm) microporous membrane (Celgard 3501) previously soaked in a saturated $NaClO_4$ (aq.) electrolytic solution was sandwiched between two of these as-coated electrodes, and the entire set-up was assembled in a standard capacitor test cell (ECC-std, EL-CELL GmbH) for tight packing and ease of measurement (Fig. 7a).

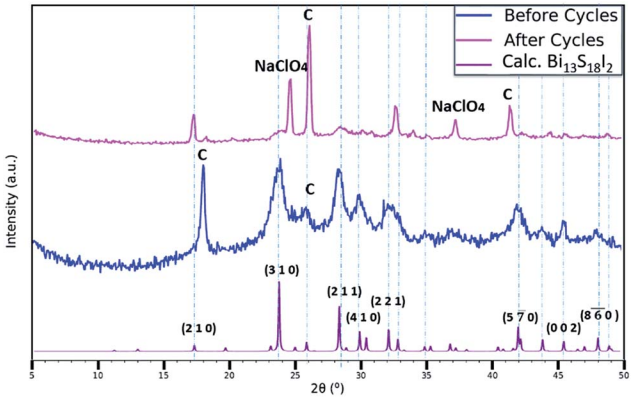

Fig. 6 Powder XRD patterns of (blue) as-prepared $Bi_{13}S_{18}I_2$ electrode on carbon cloth with PTFE and activated charcoal as additives, (magenta) $Bi_{13}S_{18}I_2$ electrode after 5000 cycles stability test and (purple) calculated powder XRD pattern of $Bi_{13}S_{18}I_2$.

Cyclic voltammetry and galvanostatic charge–discharge tests. The predominant charge storage mechanism of the $Bi_{13}S_{18}I_2$-based supercapacitor was investigated through cyclic voltammetry (CV) scans and galvanostatic charge–discharge cycles. The CV tests were performed in a voltage window ranging from 0.0 V to 0.6 V, with scan rates varying from 500 mV s^{-1} to 10 mV s^{-1} (Fig. 7c). No oxidation or reduction peaks were observed in this window, with the lowest 10 mV s^{-1} scan rate displaying a rounded-rectangular shape indicative of a predominantly non-faradaic charge storage mechanism. We note that the potential values recorded for this two-electrode device are different from the three-electrode CV measurement above, where a separate reference electrode was used. For the two-electrode measurements we carried out on the supercapacitor device, we restricted the scans to a range where we saw no faradaic peaks to ensure we are only probing EDLC-type capacitance behaviour. The non-symmetry of the CV curves at the higher scan rates are attributed to leakage current during the ultra-fast charging process and should not be attributed to a faradaic process. Such non-faradaic behaviour is characteristic of electric double layer capacitors, in contrast with so-called pseudocapacitors or supercapacitors, which rely on strong faradaic reactions to store charge.[35] The areal and specific capacitances of the assembled supercapacitor device were calculated from the CV curves according to the following equations:[43]

$$C_{\text{areal}}\ [=]\ \frac{\text{F}}{\text{cm}^2} = \frac{\int_{\Delta V} i\,\text{d}V}{\Delta V \times s \times A}$$

$$C_{\text{specific}}\ [=]\ \frac{\text{F}}{\text{g}} = \frac{\int_{\Delta V} i\,\text{d}V}{\Delta V \times s \times m}$$

where ΔV is the voltage window of the negative (cathodic) current (V), s is the constant scan rate (V s^{-1}), A is the average geometric area of the two electrodes (cm^2), and m is the combined mass of the active material on both electrodes (g). The device's areal and specific capacitances as calculated from

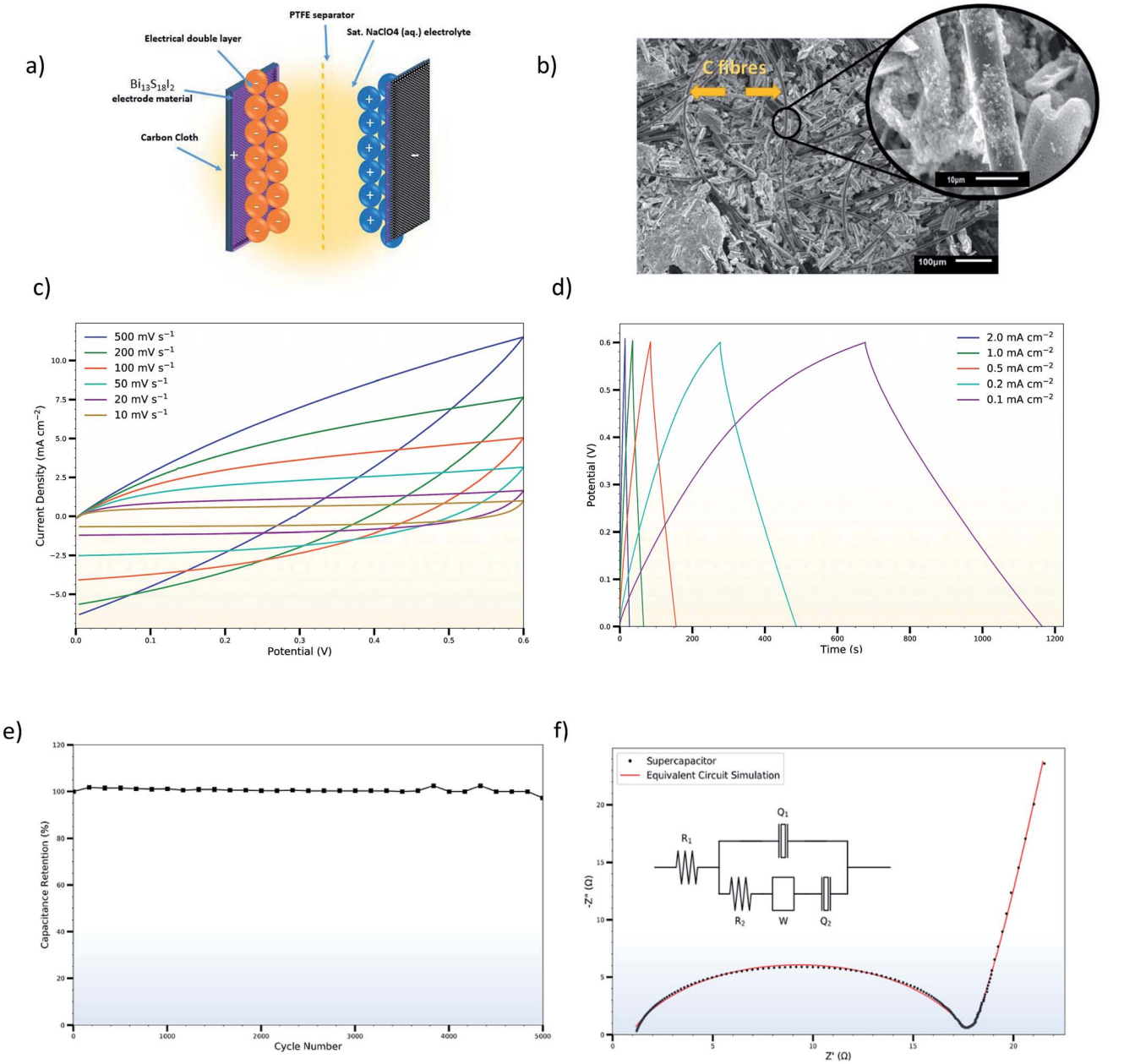

Fig. 7 (a) Schematic diagram of the EDLC in our study. (b) SEM image of an as-prepared $Bi_{13}S_{18}I_2$ electrode on carbon cloth. (c) Cyclic voltammograms of the $Bi_{13}S_{18}I_2$-based EDLC at varying scan rates. (d) Galvanostatic charge–discharge curves of the $Bi_{13}S_{18}I_2$-based EDLC. (e) Capacitance retention of the $Bi_{13}S_{18}I_2$-based EDLC over 5000 cycles. (f) Experimental (black) and simulated (red) Nyquist plots, with equivalent circuit inserted.

the CV curves spread from 53.65 mF cm^{-2} to 6.70 mF cm^{-2} and from 3.35 F g^{-1} to 0.42 F g^{-1} for scan rates increasing from 0.01 V s^{-1} to 0.5 V s^{-1}. The decrease in capacitance with increasing scan rate is a common feature of EDLCs and is caused by the different time regimes of charge transport and ion diffusion for the varying scan rates. At lower scan rates, electrolytic ions have sufficient time to diffuse into the pores of the $Bi_{13}S_{18}I_2$ active layer, increasing the charge accumulation and thus the capacitance. At higher scan rates, charge accumulation is confined to the surface of the electrodes, decreasing the electrodes' capacitances.

The galvanostatic charge–discharge measurements were similarly carried out over a 0.0–0.6 V window, with current densities varying from 2.0 mA cm^{-2} to 0.1 mA cm^{-2} (Fig. 7d). The charge–discharge curves are largely symmetric and the discharge curve displays remarkable linearity following an initial *iR* drop even at the lowest current densities, corroborating the non-faradaic, EDLC behaviour of the $Bi_{13}S_{18}I_2$ supercapacitor. The areal and specific capacitances were also calculated from the slope of the discharge curves in their linear regimes according to:

$$C_{\text{areal}}\ [=]\frac{\text{F}}{\text{cm}^2} = \frac{i}{\frac{\text{d}V}{\text{d}t}\times A}$$

$$C_{\text{specific}}\ [=]\ \frac{\text{F}}{\text{g}} = \frac{i}{\frac{\text{d}V}{\text{d}t}\times m}$$

where i is the constant current (A), $\frac{\text{d}V}{\text{d}t}$ is the slope of the discharge curve taken in the voltage range 0.0–0.1 V for consistency, and m and A retain their previously defined meanings. The device's areal and specific capacitances derived from the galvanostatic charge–discharge curves ranged from 105.34 mF cm^{-2} to 57.83 mF cm^{-2} and from 6.58 F g^{-1} to 3.61 F g^{-1} for current densities increasing from 0.1 mA cm^{-2} to 2 mA cm^{-2}. Pious and colleagues previously integrated $(CH_3NH_2)_3Bi_2I_9$ in a similar symmetric EDLC device and reported an electrode areal capacitance of 5.5 mF cm^{-2}.[20] Since our supercapacitor device employs two symmetrical electrodes in series, the electrode capacitance is equal to twice the device capacitance, or 210.68 mF cm^{-2} for our best trial at the lowest tested current density. The energy density and power density calculated from CV and galvanostatic charge–discharge measurements are summarized in Table S2,† and the energy density can be potentially increased by operating in a larger potential window. Control experiments were carried out showing that the capacitance arises from $Bi_{13}S_{18}I_2$ rather than the carbon cloth substrate or additives (Fig. S5, Table S3†). In addition, an electrode prepared from $Bi_{13}S_{18}I_2$ powder suspension was also tested, showing only about 1/10 capacitance compared to solution-processed $Bi_{13}S_{18}I_2$ electrode (Fig. S6, Table S4†). This is caused by inferior surface area of the active material $Bi_{13}S_{18}I_2$ in powder form as shown in the SEM images (Fig. S7†).

The long-term cycle stability of the $Bi_{13}S_{18}I_2$ electrodes was evaluated by performing 5000 sequential galvanostatic charge–discharge cycles at the high current density of 2 mA cm^{-2} (Fig. 7e). Even after 5000 cycles, the device retains 99.7% of its initial capacitance, demonstrating the electrodes' remarkable stability under intense electrical conditions. Moreover, SEM images of electrodes after undergoing the 5000 cycles indicate that the surface coverage of the carbon fibres with the activated $Bi_{13}S_{18}I_2$ remained largely the same after cycling (Fig. S8†). We note however that limited information can be gleaned from the SEM images, as the electrodes become heavily coated and obscured with crystallized $NaClO_4$ after use in the supercapacitor device. Still, the FTIR and Raman spectra of the electrodes after cycling display the same vibrational peaks as those of the non-tested electrodes with no significant shifts in the peak wavelengths or Raman shifts (Fig. S9†), indicating that the $Bi_{13}S_{18}I_2$ material underwent no systematic chemical degradation during the 5000 cycles. The drastically reduced intensity of the Raman spectrum for the cycled-electrodes is likely due to the thick $NaClO_4$ coating concealing the active layer. Finally, XRD was utilized to evaluate the crystal structural integrity of $Bi_{13}S_{18}I_2$ over the 5000 cycles. Fig. 6 compares the electrodes' XRD pattern both before and after the 5000 cycles with the XRD peaks calculated for the pure $Bi_{13}S_{18}I_2$ powder. Although the intensity of $Bi_{13}S_{18}I_2$'s XRD peaks also drop after cycling, the persistent peaks near 24°, 28.5°, 30°, and 32° demonstrate that the $Bi_{13}S_{18}I_2$ largely retains its crystal morphology throughout the electrochemical cycling. The extra, sharp peaks are attributed to crystalline $NaClO_4$ and exposed carbon cloth fibres.

The high capacitance performance is attributed to a combination of reasons. Firstly, the X-ray structure of $Bi_{13}S_{18}I_2$ indicates the presence of both Bi(III) and Bi(II) ions. This illustrates an ability of the Bi centre to accommodate varying charge which may explain the capacitance mechanism and would be of great interest to investigate further. The significance of Bi^{2+} is supported by the calculated band structure that was previously reported[41] and showed the lowest unoccupied states to be predominantly derived from the Bi^{2+} centres along with contributions from the immediately-adjacent Bi^{3+} and sulfur ions. As would be expected, the highest occupied states were predominantly iodide in character. Both the valence band and conduction band showed notable dispersion, at least along some directions, pointing towards an ability to delocalise and hence accommodate the added charge. Secondly, enhanced active material coverage and homogeneity have been achieved from a new solution-deposition method, which should facilitate the electrolyte diffusion into the pores. This process is also favourable for large scale solution-based manufacturing, and using flexible carbon fibre as substrate provides the possibility for roll-to-roll production methods. Finally, pH neutral $NaClO_4$ aqueous solution was used as the electrolyte, which has proven to be economic, eco-friendly and electrochemically superior with a wide potential window.[44]

Electrochemical impedance spectroscopy. Electrochemical impedance spectroscopy (EIS) was performed to characterize the physical and electrochemical processes of the $Bi_{13}S_{18}I_2$ supercapacitor in response to AC current at varying frequencies. All of the EIS measurements were conducted with a baseline potential of 0 V and an AC amplitude of 10 mV at frequencies ranging from 150 kHz to 0.1 Hz. Fig. 7f displays the imaginary (out-of-phase) impedance *versus* the real (in-phase) impedance of the $Bi_{13}S_{18}I_2$ supercapacitor in a Nyquist plot prior to the 5000 galvanostatic charge–discharge cycles. From the Nyquist plot and the Bode plot (Fig. S10†), a modified Randles equivalent circuit was fitted and shown as an inset in the Nyquist plot to analyse the resistive and capacitive elements in the supercapacitor.

The Nyquist plot shows typical EDLC-type behaviour with a semi-circle in the high-frequency regime and a linear branch in the low-frequency region. The intercept of the high-frequency end of the semi-circle with the real (Z') axis gives the value of R_1 in the equivalent circuit, representing the combined resistance due to the aqueous $NaClO_4$ electrolyte and the resistance in the current collectors, often referred to as equivalent series resistance (ESR). Since all charge migration during the charge–discharge process occurs through the electrolyte, R_1 is fitted in series with the other circuit elements and found to have a value of 0.89 Ω (Table 2). The curvature and diameter of the semi-circle are simulated with constant phase element Q_1 and resistor R_2, which are fitted in parallel to represent the two

Table 2 Electrochemical impedance spectroscopy equivalent circuit elements, for $Bi_{13}S_{18}I_2$ supercapacitor both before and after 5000 cycles

Circuit element	Value before cycles	Value after cycles
R_1	0.89 Ω	0.81 Ω
$Q_1 - n$	0.80	0.85
$Q_1 - Y_0$	22.8 μ(F $s^{-0.20}$)$^{1.25}$	13.0 μ(F $s^{-0.15}$)$^{1.18}$
R_2	16.8 Ω	19.0 Ω
$W - Y_0$	0.45 Ω^{-1} $s^{1/2}$	0.45 Ω^{-1} $s^{1/2}$
$Q_2 - n$	0.95	0.95
$Q_2 - Y_0$	71.0 m(F $s^{-0.05}$)$^{1.05}$	70.0 m(F $s^{-0.05}$)$^{1.05}$

possible behaviours of the electrolyte during the charging and discharging of the supercapacitor. At higher frequencies or shorter charging times, the electrolytic ions have insufficient time to penetrate the surface of the $Bi_{13}S_{18}I_2$ electrodes, instead forming an electrostatic capacitive layer at the surface of the electrodes highlighted in Fig. 7a. This electrostatic capacitor is modelled with a constant phase element Q_1 with an ideality factor of 0.80, signifying an imperfect capacitor, and a relatively limited Y_0 of 22.8 μ(F $s^{-0.20}$)$^{1.25}$. Y_0 is the numerical value of admittance at $\omega = 1$ rad s^{-1},[43] and $Q - Y_0$ is given by the Frequency Response Analyser EIS software as:

$$Z = \frac{1}{(Y_0 j\omega)^n}$$

where Z is the complex impedance, $j = \sqrt{-1}$, ω is the angular frequency, and n is the ideality factor. $Q - Y_0$ can be crudely approximated as the capacitance of the CPE with units of farads, but such false-equivalence has been strongly criticized.[45] Instead, we report Y_0 with its proper units of (F s^{n-1})$^{1/n}$ to avoid confusion, but note that at high n ($n \approx 1$), the approximation $Y_0 = C$ becomes increasingly valid. The non-ideality of Q_1 is attributed to surface roughness and uneven coverage of the carbon cloth with the activated $Bi_{13}S_{18}I_2$ layer, which is apparent in the SEM images of the coated electrodes (Fig. 7b). At moderate frequencies, however, the ions penetrate the electrodes' active layer, introducing R_2 with a calculated value of 16.8 Ω, representing the charge transfer resistance and the bulk resistance of the active material and electrode pores. In series with R_2 is a Warburg impedance element W, a characteristic feature of a Randles circuit that simulates the charge transport and mass diffusion of the electrolyte into the activated electrodes at mid to low frequencies. The fitted Warburg impedance gives a so-called Warburg coefficient

$$\sigma = \frac{1}{\sqrt{2}\, Y_0}$$

with $W - Y_0$ giving the admittance of the impedance at an angular frequency of 1 rad s^{-1}. Our simulated W gives $W - Y_0 =$ 0.45 Ω^{-1} $s^{1/2}$. A simple Randles circuit without the addition of Q_2 will produce linear behaviour with a 45° angle with respect to the Z' axis, characteristic of the Warburg diffusion element. The Nyquist plot for our experimental data, however, displays linear behaviour with a much steeper angle approaching 81.8°. To model this increased slope, we add a second constant phase element Q_2 in series with R_2 and W with an ideality factor $n = 0.95$ and $Y_0 = 71$ m(F $s^{-0.05}$)$^{1.05}$. The high n value suggests that Q_2 acts very nearly as an ideal capacitor, and the $Q_2 - Y_0$ closely matches the measured device capacitances derived from the CV and galvanostatic charge–discharge curves at lower scan rates or currents. We attribute this second, low-frequency regime capacitance to strong electrostatic charge storage once the electrolytic ions fully diffuse into the pores of the active $Bi_{13}S_{18}I_2$ layer.

EIS was also used to characterize the stability of the $Bi_{13}S_{18}I_2$ supercapacitor after the 5000 charge–discharge cycles. Fig. S11† compares the experimental Nyquist plot for the same $Bi_{13}S_{18}I_2$ supercapacitor before and after the cycle stability test was performed. While the low-frequency behaviour remained largely the same after cycling, R_1 decreased slightly from 0.89 Ω to 0.81 Ω, $Q_1 - Y_0$ decreased from 22.8 μ(F $s^{-0.20}$)$^{1.25}$ to 13 μ(F $s^{-0.15}$)$^{1.18}$, and R_2 increased from 16.8 Ω to 19.0 Ω. The slight decrease in the electrolyte resistance R_1 is likely due to surface film and electrolyte conditioning after multiple cycles, while the simultaneous decrease in Q_1-Y_0 and increase in R_2 may be due to mechanical wear, decreased surface area of the active layer, and trapped ions inside the surface pores of the electrodes. The largely unchanged low-frequency behaviour, however, proves the long-term electrochemical stability of the $Bi_{13}S_{18}I_2$ active layer, as long-term pore penetration and ion diffusion does not significantly affect the low-frequency diffusion and capacitive elements.

Conclusions

We have demonstrated the first facile, low-temperature, and solution-processing synthesis of both powder and thin-film samples of a relatively-unexplored bismuth chalcohalide material, $Bi_{13}S_{18}I_2$. The optimal ratio for the $Bi(xt)_3$ and BiI_3 precursors has been studied and established, and the crystal structure of deposited thin films match the theoretical pattern calculated by powder XRD measurements. The elemental composition of $Bi_{13}S_{18}I_2$ has been verified by XPS, and the direct and indirect band gap values (0.68 eV and 0.92 eV, respectively) are characterized *via* diffuse reflectance measurements. The energy level diagram for $Bi_{13}S_{18}I_2$ has been estimated based on electrochemistry techniques, using solid state $Bi_{13}S_{18}I_2$ on FTO as the working electrode. In an extensive supercapacitor device study, $Bi_{13}S_{18}I_2$ has been employed as the active material in an EDLC device, and a simple and economical electrode fabrication process has been demonstrated. Optimization of the active material deposition *via* solution-processing methodology and choice of electrolyte solution have together enhanced the EDLC performance. Utilizing a high mass loading (7–8 mg cm^{-2}) of active material and saturated aqueous sodium perchlorate as the electrolyte, we have achieved a non-faradaic EDLC with a superior areal capacitance of 210.68 mF cm^{-2} and an excellent 99.7% capacitance retention over 5000 charge–discharge cycles. The EDCL mechanism is supported by the lack of any redox peaks in the cyclic voltammogram and a largely linear galvanostatic discharge curve, suggesting the capacitance derives from the transfer of delocalised electrons,[46] a mechanism which is also consistent with the reported band structure.[41] For the

first time, we have proven that $Bi_{13}S_{18}I_2$-based electrodes can be fabricated from solution and integrated in low-cost, commercially-viable supercapacitors featuring promising energy storage capabilities and excellent long-term cycle stability.

Experimental

Materials

All reagents were obtained from commercial suppliers (Acrōs Organics, Sigma Aldrich, Fluka) and used as received, unless otherwise stated. Solvents used were of analytical grade (Sigma Aldrich, Fisher Scientific, VWR Chemicals, and Cambridge Isotope Laboratories). The following compounds and solvents were used in this experiment: bismuth(III) nitrate pentahydrate (98%), potassium xanthate (96%), bismuth iodide (99%), hydrochloric acid (37%), *n*,*n*-dimethylformamide (99.8%), dimethyl sulfoxide (>99%), deuterated acetone (99.9%), barium sulfide (99%), dichloromethane (>99.8%), ferrocene (98%), tetrabutylammonium hexafluorophosphate (98%), activated charcoal, PTFE powder (particle size < 1 μm), butanol, and ethanol were purchased from Sigma-Aldrich. Titania paste was obtained from Greatcell Solar (18NRT-Active Opaque). ^{1}H NMR spectra were recorded in deuterated acetone for potassium xanthate and bismuth xanthate on a 500 MHz Bruker AV III (Ava 500) at a constant temperature of 300 K. The chemical shifts are reported in ppm using $SiMe_4$ as the reference.

Material characterizations

Powder X-ray diffraction (PXRD) was performed on a Bruker (D8 Advance) diffractometer with monochromatic Cu-Kα radiation and wavelength of 1.5406 Å. The measurements were performed at room temperature over a 2-theta scattering angle of 5–60°, with increments of 0.1° on the 2-theta scale.

X-ray photoelectron spectra were acquired in a Thermo Scientific (VG Sigma Probe) XPS spectrometer using monochromatic Al-Kα as the source of X-rays. Scanning electron microscopy was performed by Gylen Odling using a Zeiss (SIGMA HD VP) Field Emission-SEM. Diffuse reflectance measurements for powder and thin film samples of $Bi_{13}S_{18}I_2$ were recorded on a Jasco (V-670) spectrophotometer with Spectra Manager software. The powder sample was prepared by mixing thin film material with a barium sulphite ($BaSO_4$) matrix in a 5 : 95 weight ratio. The Kubelka–Munk function was used to analyse the diffuse reflectance data, and Tauc plots were constructed to obtain the optical E_g for direct and indirect transitions. Cyclic voltammetry measurements were performed using a three-electrode cell with the spin-coated $Bi_{13}S_{18}I_2$ on FTO-coated glass on top of a mesoporous TiO_2 layer as the working electrode. The sample was placed in dichloromethane, using tetrabutylammonium hexafluorophosphate (0.3 M) as the supporting electrolyte, platinum as a counter electrode, and a Ag/AgCl reference electrode. The cyclic voltammetry was recorded in an Autolab (Type III) potentiostat at linear scan rates of 0.5 V s^{-1}, 0.2 V s^{-1}, and 0.1 V s^{-1}. The samples were cycled 5 times at each sweep speed and the average obtained, with degassing of the solvent under N_2 before each measurement. The redox process of the ferrocenium/ferrocene couple was recorded to be used as the internal standard. The FT-IR spectra were recorded using Perkin Elmer FT-IR Spectrum 65 range from 400 to 4000 cm^{-1}, with resolution of 4 cm^{-1}. Raman spectra were acquired from a Renishaw InVia Raman Microscope with the excitation laser wavelength of 785 nm, with a spectral resolution of roughly 1 cm^{-1}.

EDLC studies

The precursor solution of $Bi_{13}S_{18}I_2$ was made by mixing BiI_3 and $Bi(xt)_3$ in a molar ratio of 1 : 18 together with activated charcoal powder and PTFE powder in 1 mL DMF as the solvent to make a final $Bi_{13}S_{18}I_2$: charcoal : PTFE mixture with a weight ratio of 85 : 10 : 5 (total mass: 565.7 mg). The resulting suspended solution was sonicated until homogenized, and around 200 μL was drop-coated onto 1 cm^2 of conductive carbon cloth (ELAT, NuVant Systems Inc.) substrate. Absorbing tissue was placed underneath the carbon cloth to absorb excess solution in order to maximize surface coverage and film homogeneity of the carbon cloth while reducing the mass loading of the active $Bi_{13}S_{18}I_2$ layer. The coated electrodes were then annealed at 150 °C for 1 h on a hotplate. The dimension of carbon cloth was measured under an optical microscope, and the mass of active material was determined by subtracting the mass of carbon cloth (density: 13 mg cm^{-2}, shown on the product manual) from the total mass of the dried electrode (estimated error: ±0.4 mg based on multiple repeat measurements). For the cyclic voltammetry and galvanostatic charge–discharge tests, a total of 16.0 mg of the activated $Bi_{13}S_{18}I_2$ layer was loaded onto two carbon cloths (dimensions: 10.2 mm × 10.9 mm, 9.8 mm × 10 mm). For the 5000 cycles and EIS testing, a total of 14.7 mg was loaded onto two carbon cloths (dimensions: 11.3 mm × 11.0 mm, 10.7 mm × 10.7 mm). When assembling the EDLC, two coated electrodes were separated by a thin polymer separator (Celgard 3501) pre-soaked in a saturated sodium perchlorate aqueous electrolyte solution and then sandwiched in a symmetrically assembled capacitor test cell (ECC-std, EL-CELL GmbH). Electrochemical measurements were carried out by connecting the test cell in a two-electrode configuration to an Autolab potentiostat with FRA2 module using General Purpose Electrochemical System (GPES) and Frequency Response Analyser (FRA) software. The equivalent circuit modelling was carried out with the FRA software. The control experiments with electrodes deposited from $Bi_{13}S_{18}I_2$ suspension were achieved by dispersing $Bi_{13}S_{18}I_2$: charcoal : PTFE mixture in 1 mL ethanol, with same weight ratio and a total mass of 529.3 mg.

Conflicts of interest

The authors state there are no conflicts to declare.

Acknowledgements

We thank the EPSRC Multiscale Tuning of Interfaces and Surfaces for Energy Applications consortium for a flexible-funding project, and the School of Chemistry, University of

Edinburgh for financial support. Open data: http://dx.doi.org/10.7488/ds/2479. We thank School of Physics and Astronomy in the University of Edinburgh for performing the SEM measurements, with help from Dr Andrew Schofield. We thank Dr Andrey Gromov for the help of performing Raman measurements. We thank Dr Ronald Brown for help in performing XPS measurements. We thank Prof. Andrew Mount and Dr Dimitrios Kampouris for the fruitful discussion. KA thanks the University of Chicago/University of Edinburgh student exchange scheme for support.

Notes and references

1 M. A. Hannan, M. M. Hoque, A. Mohamed and A. Ayob, *Renewable Sustainable Energy Rev.*, 2017, **69**, 771–789.
2 M. B. Tayel, M. M. Soliman, S. Ebrahim and M. E. Harb, *J. Electron. Mater.*, 2016, **45**, 820–828.
3 C. Guan, X. Liu, W. Ren, X. Li, C. Cheng and J. Wang, *Adv. Energy Mater.*, 2017, **7**, 1602391.
4 G. Wang, L. Zhang and J. Zhang, *Chem. Soc. Rev.*, 2012, **41**, 797–828.
5 L. L. Zhang and X. S. Zhao, *Chem. Soc. Rev.*, 2009, **38**, 2520–2531.
6 Z. Yu, L. Tetard, L. Zhai and J. Thomas, *Energy Environ. Sci.*, 2015, **8**, 702.
7 Z. S. Iro, C. Subramani and S. S. Dash, *Int. J. Electrochem. Sci.*, 2016, **11**, 16028.
8 L. Yu and G. Z. Chen, *J. Power Sources*, 2016, **326**, 604–612.
9 Z. Ran, X. Wang, Y. Li, D. Yang, X. G. Zhao, K. Biswas, D. J. Singh and L. Zhang, *npj Comput. Mater.*, 2018, **4**, 14.
10 L. C. Lee, T. N. Huq, J. L. Macmanus-Driscoll and R. L. Z. Hoye, *APL Mater.*, 2018, **6**, 084502.
11 L. M. Wu, X. T. Wu and L. Chen, *Coord. Chem. Rev.*, 2009, **253**, 2787–2804.
12 R. Mohan, *Nat. Chem.*, 2010, **2**, 336.
13 T. Li, Q. Wang, G. S. Nichol, C. A. Morrison, H. Han, Y. Hu and N. Robertson, *Dalton Trans.*, 2018, **47**, 7050–7058.
14 T. Li, Y. Hu, C. Morrison, W. Wu, H. Han and N. Robertson, *Sustainable Energy Fuels*, 2017, **1**, 308–316.
15 A. J. Lehner, D. H. Fabini, H. A. Evans, C. A. Hébert, S. R. Smock, J. Hu, H. Wang, J. W. Zwanziger, M. L. Chabinyc and R. Seshadri, *Chem. Mater.*, 2015, **27**, 7137–7148.
16 N. A. Yelovik, A. V Mironov, M. A. Bykov, A. N. Kuznetsov, A. V Grigorieva, Z. Wei, E. V Dikarev and A. V Shevelkov, *Inorg. Chem.*, 2016, **55**, 4132–4140.
17 Z. Zhang, X. Li, X. Xia, Z. Wang, Z. Huang, B. Lei and Y. Gao, *J. Phys. Chem. Lett.*, 2017, **8**(17), 4300–4307.
18 T. Singh, A. Kulkarni, M. Ikegami and T. Miyasaka, *ACS Appl. Mater. Interfaces*, 2016, **8**(23), 14542–14547.
19 X. W. Tong, W. Y. Kong, Y. Y. Wang, J. M. Zhu, L. B. Luo and Z. H. Wang, *ACS Appl. Mater. Interfaces*, 2017, **9**(22), 18977–18985.
20 J. K. Pious, M. L. Lekshmi, C. Muthu, R. B. Rakhi and V. C. Nair, *ACS Omega*, 2017, **9**(22), 18977–18985.
21 L. Ma, Q. Zhao, Q. Zhang, M. Ding, J. Huang, X. Liu, Y. Liu, X. Wu and X. Xu, *RSC Adv.*, 2014, **4**, 41636–41641.
22 J. Jiang, X. Zhang, P. Sun and L. Zhang, *J. Phys. Chem. C*, 2011, **115**(42), 20555–22056.
23 Y. Huang, H. Li, M. S. Balogun, W. Liu, Y. Tong, X. Lu and H. Ji, *ACS Appl. Mater. Interfaces*, 2014, **6**(24), 22920–22927.
24 R. L. Z. Hoye, L. C. Lee, R. C. Kurchin, T. N. Huq, K. H. L. Zhang, M. Sponseller, L. Nienhaus, R. E. Brandt, J. Jean, J. A. Polizzotti, A. Kursumović, M. G. Bawendi, V. Bulović, V. Stevanović, T. Buonassisi and J. L. MacManus-Driscoll, *Adv. Mater.*, 2017, **27**, 1702176.
25 J. Song, J. Yuan, F. Xia, J. Liu, Y. Zhang, Y. L. Zhong, J. Zheng, Y. Liu, S. Li, M. Zhao, Z. Tian, R. A. Caruso, K. P. Loh and Q. Bao, *Adv. Electron. Mater.*, 2016, **2**(5), 1600077.
26 G. Nie, X. Lu, J. Lei, L. Yang and C. Wang, *Electrochim. Acta*, 2015, **154**, 24–30.
27 S. X. Wang, C. C. Jin and W. J. Qian, *J. Alloys Compd.*, 2014, **615**, 12–17.
28 M. Ciszewski, A. Mianowski, P. Szatkowski, G. Nawrat and J. Adamek, *Ionics*, 2015, **21**(2), 557–563.
29 X. Yang, S. Tian, R. Li, W. Wang and S. Zhou, *Sens. Actuators, B*, 2017, **241**, 210–216.
30 Z. Zhao, Y. Ye, W. Zhu, L. Xiao, B. Deng and J. Liu, *Chin. Chem. Lett.*, 2018, **29**, 629–632.
31 N. M. Shinde, Q. X. Xia, J. M. Yun, R. S. Mane and K. H. Kim, *ACS Appl. Mater. Interfaces*, 2018, **10**, 11037–11047.
32 N. T. Hahn, A. J. E. Rettie, S. K. Beal, R. R. Fullon and C. B. Mullins, *J. Phys. Chem. C*, 2012, **116**(47), 24878–24886.
33 A. M. Ganose, K. T. Butler, A. Walsh and D. O. Scanlon, *J. Mater. Chem. A*, 2016, **4**, 2060–2068.
34 H. Kunioku, M. Higashi and R. Abe, *Sci. Rep.*, 2016, **6**, 32664.
35 B. E. Conway, *Electrochemical Supercapacitors Scientific Fundamentals and Technological Applications*, Springer, USA, 1999.
36 J. Ni, X. Bi, Y. Jiang, L. Li and J. Lu, *Nano Energy*, 2017, **34**, 356–366.
37 Y. Yan, Y. Xu, S. Lei, X. Ou, L. Chen, J. Xiong, Y. Xiao and B. Cheng, *Dalton Trans.*, 2018, **47**, 3408–3416.
38 C.-H. Ho, Y.-H. Chen, Y.-K. Kuo and C. W. Liu, *Chem. Commun.*, 2017, **53**, 3741–3744.
39 B. Xu, T. Feng, M. T. Agne, Q. Tan, Z. Li, K. Imasato, L. Zhou, J. H. Bahk, X. Ruan, G. J. Snyder and Y. Wu, *Angew. Chem., Int. Ed.*, 2018, **57**, 2413–2418.
40 M. Vigneshwaran, T. Ohta, S. Iikubo, G. Kapil, T. S. Ripolles, Y. Ogomi, T. Ma, S. S. Pandey, Q. Shen, T. Toyoda, K. Yoshino, T. Minemoto and S. Hayase, *Chem. Mater.*, 2016, **28**, 6436–6440.
41 R. Groom, A. Jacobs, M. Cepeda, R. Drummey and S. E. Latturner, *Chem. Mater.*, 2017, **29**, 3314–3323.
42 F. N. Crespilho, V. Zucolotto, J. R. Siqueira, A. J. F. Carvalho, F. C. Nart and O. N. Oliveira, *Int. J. Electrochem. Sci.*, 2006, **1**, 151–159.
43 E. Barsoukov and J. R. Macdonald, *Impedance Spectroscopy Theory, Experiment and Applications*, John Wiley & Sons, USA, 2nd edn, 2018.
44 H. Tomiyasu, H. Shikata, K. Takao, N. Asanuma, S. Taruta and Y.-Y. Park, *Sci. Rep.*, 2017, **7**, 45048.
45 P. Żółtowski, *J. Electroanal. Chem.*, 1998, **443**, 149–154.
46 J. Xie, P. Yang, Y. Wang, T. Qi, Y. Lei and C.-M. Lia, *J. Power Sources*, 2018, **401**, 213–223.

